J Comput Electron (2016) 15:16–26
DOI 10.1007/s10825-016-0792-7

Modulation doping and energy filtering as effective ways to improve the thermoelectric power factor

Neophytos Neophytou[1] · **Mischa Thesberg**[2]

Published online: 29 January 2016

Abstract Thermoelectric (TE) materials have undergone revolutionary progress over the last 20 years. The thermoelectric figure of merit ZT, which quantifies the ability of a material to convert heat into electricity has more than doubled compared to traditional values of $ZT \sim 1$, reaching values even beyond $ZT \sim 2$ in some instances. These improvements are mostly attributed to drastic reductions of the thermal conductivity in nanostructured materials and nanocomposites. However, as thermal conductivities in these structures approach the amorphous limit, any further benefits to ZT must be achieved through the improvement of the thermoelectric power factor. In this work we review two of the most promising avenues to increase the power factor, namely (i) modulation doping and (ii) electron energy filtering, and present a computational framework for analysis of these mechanisms for two example cases: low-dimensional gated Si nanowires (electrostatically achieved doping), and superlattices (energy filtering over potential barriers). In the first case, we show that a material with high charge density, but free of ionized impurities, can provide up to a five-fold thermoelectric power factors increase compared to the power factor of the doped material, which highlights the benefits of modulation doping, or gating of materials. In the second case, we show that optimized construction of energy barriers within a superlattice material geometry can improve the power factor by up to $\sim 30\,\%$. This paper is intended to be a review of our main findings with regards to efforts to improve the thermoelectric power factor through modulation doping and energy filtering.

Keywords Thermoelectricity · Thermoelectric power factor · Seebeck coefficient · Modulation doping · Energy filtering · Atomistic calculations · Quantum transport

1 Introduction

The ability of a material to convert heat into electricity is measured by the dimensionless figure of merit $ZT = \sigma S^2 T/(\kappa_e + \kappa_l)$, where σ is the electrical conductivity, S is the Seebeck coefficient, and κ_e and κ_l are the electronic and lattice parts of the thermal conductivity, respectively. Traditionally ZT has been constrained to values of $ZT \sim 1$ or below, corresponding to $\sim 10\,\%$ of the Carnot efficiency [1]. Recently, large improvements in the ZT up to values of $ZT \sim 2.2$ have been demonstrated in nanostructures [2–6]. Much of this enhancement is owed to large reductions in their thermal conductivity compared to bulk material values. Thermal conductivities were reduced to $\kappa_l = 1 - 2\,\mathrm{W/mK}$, values close to or even below the amorphous limit [7–15]. It has very recently become evident, however, that benefits from κ_l reduction are reaching their limits, and further increases of ZT can only be achieved through improvements in the power factor σS^2 [16,17].

Similar benefits from power factor (σS^2) improvements, however, have not yet been realized. This is attributed to the adverse interdependence of the electrical conductivity and Seebeck coefficient via the carrier density, which proves very difficult to overcome. Figure 1a–c shows the dependence of the conductivity, the Seebeck coefficient, and the power factor, respectively, versus the reduced Fermi level $\eta_F = E_F - E_C$, which dictates the carrier density. The

✉ Neophytos Neophytou
N.Neophytou@warwick.ac.uk

[1] School of Engineering, University of Warwick, Coventry CV4 7AL, UK

[2] Institute for Microelectronics, Technical University of Vienna, Vienna, Austria

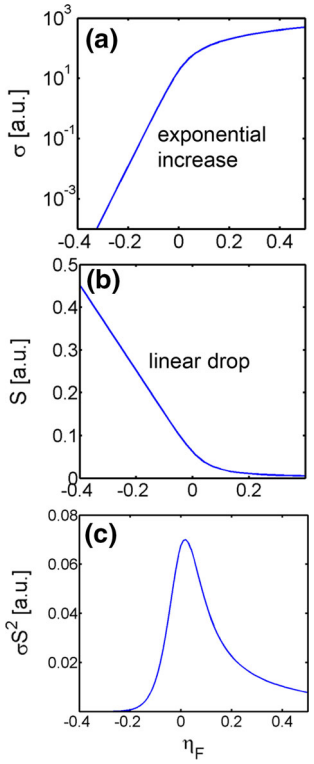

Fig. 1 The dependence of the electrical conductivity (**a**), the Seebeck coefficient (**b**) and the thermoelectric power factor (**c**), on the reduced Fermi level $\eta_F = E_F - E_C$, where E_C is the conduction band and E_F is the Fermi level

electrical conductivity increases exponentially with η_F (as it increases the carrier density exponentially), the Seebeck coefficient drops linearly with η_F, which forces the power factor σS^2 to a maximum value, that has proved resistant over the years to further increase. To achieve power factor improvements, some of the initial efforts by Hicks and Dresselhaus suggested the use of low-dimensional channels, which include sharp features in their density of states that are beneficial to the Seebeck coefficient [18]. The idea was that, in these dimensionally limited structures, the electrical conductivity would not suffer substantially, and that the ensuing improvement in the Seebeck coefficient would ultimately increase the power factor. Mahan and Sofo have further shown theoretically that thermoelectric (TE) energy conversion through a single energy level (0D channel) can reach the Carnot efficiency when κ_l is zero [19]. Despite large efforts by the TE community over the last few decades, however, significant power factor enhancements due to low-dimensional effects has not materialized. Clearly the adverse interplay between the Seebeck coefficient and the electrical conductivity has proved more complicated than originally suspected. This complexity is further bolstered by the energy dependence of scattering mechanisms.

Current research efforts in TEs are manifold. The engineering of the density of states of low-dimensional materials through quantum confinement [20] is still a topic of interest, but other strategies such as bandstructure engineering [21–24], modulation doping [25–31], introducing energy resonances in the density of states [32,33], and energy filtering in nanocomposites and superlattices [34–45] are being actively pursued. The common objective of these disparate methods is to engineer the bandstructure and transport in TE materials such that either the electrical conductivity or the Seebeck coefficient are tuned independently, or increased simultaneously, which could maximize σS^2. However, although theoretical works indicate that power factor improvements are possible, to-date experiments do not commonly demonstrate significant improvements.

In this review paper, we present two example studies of the main and most promising strategies to achieve large thermoelectric power factors, namely: (i) remote doping (electrostatic doping through gating in this case), and (ii) energy filtering in superlattice geometries. In the first case we present atomistic tight-binding self-consistent simulations of the thermoelectric power factor in gated versus doped Si nanowires. The motivation behind remote doping is to achieve high carrier densities in a TE material free of ionized impurities to improve electronic transport. In the second case study, we present theoretical calculations of the benefits of thermoelectric transport through superlattices composed of potential wells and barriers on the power factor. In this approach, the goal is to achieve improved energy filtering using the potential wells in the material, which improves the Seebeck coefficient. Here we review our theoretical efforts to optimize the energy filtering process by employing the Non-Equilibrium Green's function quantum transport formalism, including the effects of electron phonon scattering, and discuss 1D and 2D geometries.

The paper is organized as follows: In Sect. 2 we present our simulation methodology and examine the benefits from electrostatic modulation doping in Si nanowires. In Sect. 3 we describe our simulation methodology and examine the benefits from energy filtering. In Sect. 4 we discuss the results and further approaches, and in Sect. 5 we conclude.

2 Electrostatic gating benefits to the power factor of nanowires

The thermoelectric power factor σS^2 peaks at high carrier concentrations around $10^{19} - 10^{20}/\text{cm}^3$, and in most cases this is achieved by doping. Doping at such high levels, however, introduces strong ionized impurity scattering (IIS) on charged carriers, and severely limits mobility and electronic conductivity. Figure 2 shows mobility calculations of a p-type Si nanowire in the [111] transport direction for the phonon-limited case (dashed line), and the phonon plus ionized impurity limited case (solid line). Indeed, the

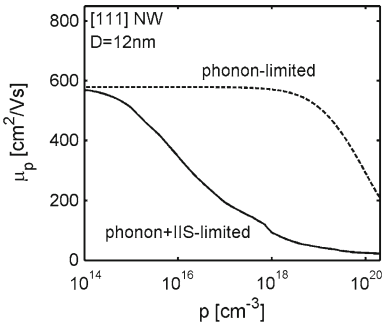

Fig. 2 The mobility of the $D = 12$ nm [111] nanowire (NW) versus carrier density for two different channel situations: (i) Phonon-limited mobility (*black-dashed line*). (ii) Phonon scattering and ionized impurity scattering (IIS) are considered (*black-solid line*)

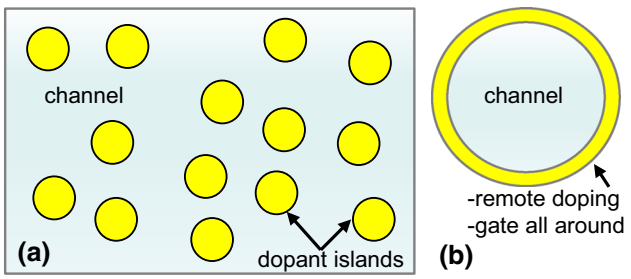

Fig. 3 Schematics of modulation doping techniques. **a** Doped islands, or highly doped regions within an undoped material provide remote doping to the active thermoelectric material region. **b** Remote doping or electrostatic doping gating through gating in a nanowire channel geometry

phonon-limited mobility, which would be achieved by modulation doping, is almost an order of magnitude higher compared to the ionized-impurity-limited mobility. With regards to its influence on the thermoelectric performance, in Ref. [21] we compared the phonon-limited to the phonon plus IIS thermoelectric power factor in Si nanowires (NWs) and demonstrated that both the power factor and ZT could be a factor of $\sim 4\times$ lower in the presence of IIS. Thus, modulation doping has been suggested as a possible way to achieve the required high carrier densities, while mitigating the detrimental effects of ionized dopants in the channel [25,26].

Indeed, several experimental works have demonstrated strong electric field modulation of the conductivity and the thermopower, with orders of magnitude improvement using modulation doping techniques, e.g. remote doping as shown in Fig. 3a where dopant islands are introduced within a material matrix [25,26], electrostatic gating [27,46–48], where a gate (or doped layer) is placed around a nanowire as shown in Fig. 3b, etc., but in all cases the quantitative improvement that was achieved over doped materials was only modest [25–27,46–48]. In the best case, they report power factors similar to those of doped bulk materials [27]. It is, thus, difficult to examine whether gating could actually provide higher power factors, what the magnitude of the improvement would be, and at which channel size these improvements could be achieved.

As a computational example of modulation doping for the purposes of this review, we compute the thermoelectric power factor of gated Si nanowires of a diameter of 12 nm and compare it to the power factor of a doped nanowire. We qualitatively and quantitatively examine their performance differences, and indeed, show that remarkable power factor improvements up to $\sim 5\times$ can be achieved in the gated channels. Gating is a similar situation as in transistor devices, with the exception that in this case we form an accumulation, rather than an inversion layer of charge, which is less susceptible to surface roughness scattering as we show below. In the modulated doping nanowire case, the electric field from gating or from remote dopants can reach far into the enclosed channel volume. This creates high mobility carriers in the accumulation layer that forms, which improves the TE power factor. As the diameter increases, the bulk volume of the material contributes less and less to the overall power factor. However, in gate-all-around nanowires we have shown in Ref. [28] that benefits can be realized for nanowires with diameters up to $D \sim 40$ nm because the gate can effectively create an accumulation layer stretching deep into the core of the NW. A nanowire would be a good candidate for a modulated doping material due the tuneability of its diameter, since small diameters reduce the thermal conductivity [7,8]. In principle, one could extend the NW to bulk like material by placing arrays of gated NWs.

The complete computational model we employ is described in Fig. 4. There are four steps in the computation [49]: (i) The first step is the calculation of the electronic bandstructure of the nanowire channel. For this we employ the $sp^3d^5s^*$ tight-binding (TB) atomistic model [50,51]. The Schrodinger equation is solved only in the Si channel, whereas the oxide is only included in the electrostatics of the device. The TB model assumes hydrogen passivated edge atoms using an effective passivation scheme described in Ref. [52]. Here we consider only the [111] p-type NW channel, which indicates significantly higher performance compared to the [100] and the [110] channels [53], but the conclusions are generally valid for all NW channels [28]. (ii) The second step involves the calculation of the charge density using equilibrium statistics. The k-states of the bandstructure are filled according to the Fermi level, which is assumed to be uniform along the length of the device. The position of the Fermi level determines the charge density (Fig. 4b). (iii) The third step is the solution of a 2D Poisson equation in the cross section of the NW. A gate all around geometry is used, with 1.1 nm SiO_2 as the gate insulator. When solving the Poisson equation we include the carrier distribution in the channel (as indicated in Fig. 4c), which is determined by the coefficients of the eigenvectors of the various k-states. These first three steps are solved self-consistently since the band-

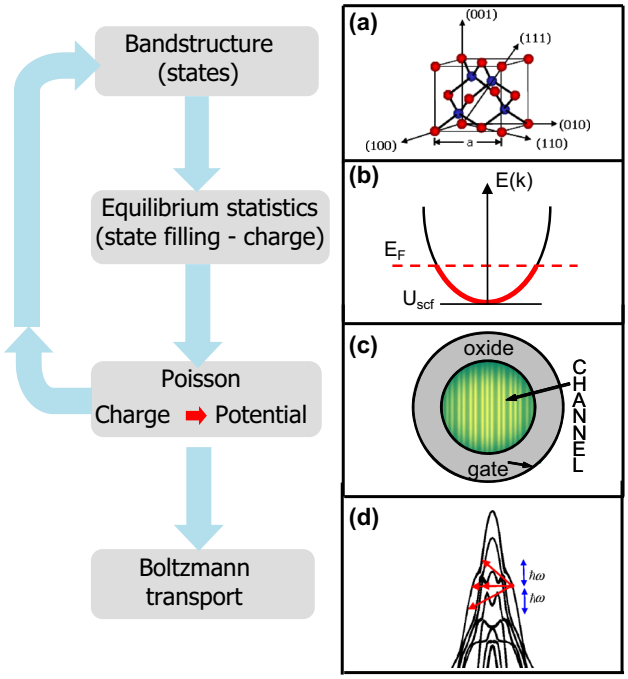

Fig. 4 Simulation procedure steps (from *top to bottom*). **a** The NW bandstructure is calculated using the $sp^3d^5s^*$ tight-binding model. **b** Equilibrium statistics are used to calculate the charge distribution in the NW. **c** The charge is self-consistently coupled to a 2D Poisson equation to obtain the electrostatic potential in the cross section of the wire. **d** Upon convergence, Boltzmann transport theory is used for mobility calculations. (Examples of relevant valence band scattering mechanisms are shown)

structure is a function of the potential profile in the channel. (iv) Once self-consistency is achieved, we use the linearized Boltzmann transport formalism to extract the thermoelectric coefficients including all relevant scattering mechanisms, i.e. acoustic phonons, optical phonons, surface roughness scattering (SRS), and ionized impurity scattering (IIS) as described in detail in Refs. [21,49]. IIS is only applied for doped/non-gated structures. We perform the above procedure for a series of gate biases, increasing the charge density and driving the channel from depletion to accumulation.

Within the linearized Boltzmann transport theory, the electrical conductivity, Seebeck coefficient, and the electronic part of the thermal conductivity are given by the following expressions:

$$\sigma = q_0^2 \int_{-\infty}^{E_0} dE \left(-\frac{\partial f_0}{\partial E}\right) \Xi(E), \tag{1a}$$

$$S = \frac{q_0 k_B}{\sigma} \int_{-\infty}^{E_0} dE \left(-\frac{\partial f_0}{\partial E}\right) \Xi(E) \left(\frac{E - E_F}{k_B T}\right), \tag{1b}$$

The energy E integration over the derivative of the Fermi distribution $f_0(E)$ is performed from the valence band edge E_0 though all energies. $\Xi(E)$ is the transport distribution function (TD) defined as [19,21]:

$$\Xi(E) = \frac{1}{A} \sum_{k_x,n} v_n^2(k_x)\, \tau_n(k_x)\, \delta(E - E_n(k_x)) = \frac{1}{A} \sum_{n} v_n^2(E)\, \tau_n(E)\, g_{1D}^n(E). \tag{2}$$

Here $v_n(E) = \frac{1}{\hbar}\frac{\partial E_n}{\partial k_x}$ is the bandstructure velocity of subband n with dispersion E_n, $\tau_n(k_x)$ is the momentum relaxation time for a carrier with wavenumber k_x in subband n,

$$g_{1D}^n(E) = \frac{1}{2\pi\hbar}\frac{1}{v_n(E)} \tag{3}$$

is the density of states for the 1D subbands (per spin), and A is the cross sectional area of the NW.

For SRS we assume a 1D exponential autocorrelation function for the roughness, with roughness amplitude $\Delta_{\rm rms} = 0.48$ nm and roughness correlation length $L_C = 1.3$ nm [54]. In the case of doped nanowires, with a flat potential in their cross section, surface roughness is assumed to cause a band edge shift due to diameter modulation. The scattering strength is derived from the shift in the band edge with quantization $\frac{\Delta E_0}{\Delta D}$ [55,56], and the transition rate here is given as:

$$S_{n,m}^{SRS}(k_x, k_x') = \frac{2\pi}{\hbar}\left(\frac{q_0 \Delta E_0}{\Delta D}\right)^2 \left(\frac{2\sqrt{2}\Delta_{rms}^2 L_C}{2 + q_x^2 L_C^2}\right) \times \delta\left(E_m(k_x') - E_n(k_x)\right), \tag{4}$$

where $q_x = k_x - k_x'$. The band edge variation is the dominant SRS mechanism in ultra-scaled channels and results in the low-field mobility in ultra-thin nanostructures to follow a D^6 behavior, where D is the confinement length scale, in this case the diameter of the channel. Note, however, that for $D > 10$ nm, this effect is weak. In addition, for NWs with flat potential in their cross section, in which case transport mostly happens within the NW core, SRS is in general weak.

For SRS in the gated NWs, we follow the usual way of deriving the scattering matrix element and scattering rates from the strength of the radial electric field in the channel [57]. The transition rate is given by:

$$S_{n,m}(k_x, k_x') = \frac{2\pi}{\hbar}\left|\langle F_f \left|\varepsilon_{eff}(r)\right| F_i\rangle\right|^2 \frac{\Delta_{rms}^2 L_C}{(2 + q_x^2 L_C^2)} \times \delta\left(E_m(k_x') - E_n(k_x)\right) \tag{5}$$

Above, $\delta(\cdot)$ is the Dirac-delta function which denotes energy conservation, $F_{f,i}$ are the final/initial bound states in the transverse plane (NW cross section), ε_{eff} is the radial gate-induced electric field in the NW cross section, and $q_x = k_x - k_x'$.

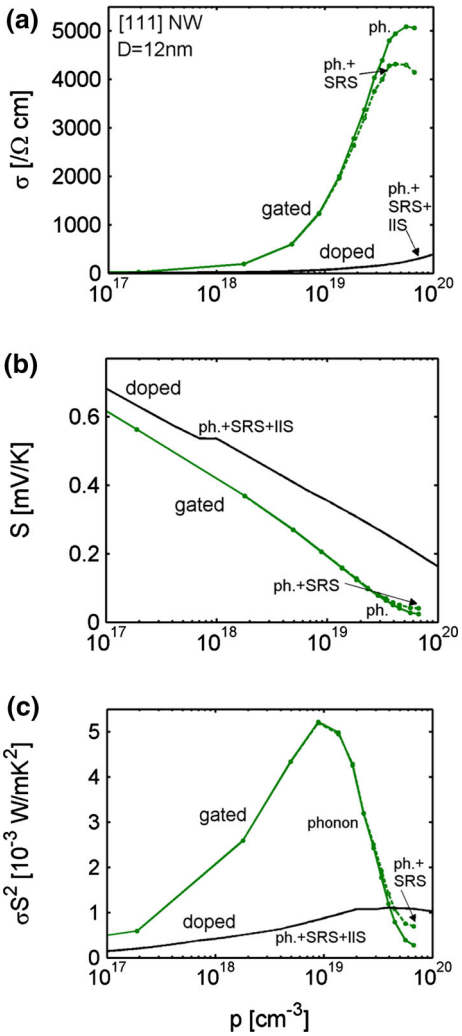

Fig. 5 The thermoelectric coefficients of the $D = 12\,\text{nm}$ [111] nanowire versus carrier density. **a** The electrical conductivity. **b** The Seebeck coefficient. **c** The power factor. Three different channel situations are shown: (i) Gated NW under phonon scattering-limited considerations (*green-dot-solid line*). (ii) Gated NW under phonon scattering and SRS considerations (*green-dot-dashed line*). (iii) Doped (non-gated) NW under phonon scattering, IIS, and SRS considerations (*black-solid line*)

The required charge density for high thermoelectric power factor is around $10^{19}/\text{cm}^3 - 10^{20}/\text{cm}^3$. The advantage in achieving such high carrier concentration by gating rather than doping, lies in the fact that ionized impurity dopants will significantly reduce the electrical conductivity [58]. Figure 5a compares the electrical conductivity versus carrier concentration of the [111] NW with diameter $D = 12\,\text{nm}$ for these two channels. Three cases are depicted: (i) Gated NW with phonon-limited scattering transport considerations (green-dot-solid line); (ii) Gated NW with phonon scattering and surface-roughness-scattering (SRS) transport considerations (green-dot-dashed line); (iii) Doped NW with phonon scattering, SRS, and ionized impurity scattering (IIS) transport considerations (black-solid line). Due to the absence of ionized impurity scattering, the electrical conductivity of the gated channel largely surpasses that of the doped channel. In the case of the doped channel, where IIS (and SRS) is additionally considered in the calculations, the conductivity significantly drops. An important point to be mentioned here is that including SRS on top of phonon scattering affects the conductivity of the gated channel only to a small degree, and that only at concentrations above $p = 3 \times 10^{19}/\text{cm}^3$ (dashed versus solid green-dot lines). The reason why SRS is weak is that the electric field to achieved a hole *accumulation* layer is relatively weak. The electric field at the surface of the NW for the optimal power factor case in these simulations was deduced to be $\varepsilon_{eff}(r = D/2) \sim 0.2\,\text{MV/cm}$. This value is smaller compared to the electric field needed to achieve an *inversion* layer, as for example in transistor devices. In that case the field is $\varepsilon_{eff} > 0.3\,\text{MV/cm}$ [59]. SRS begins to become detrimental to the conductivity for even larger fields, $\varepsilon_{eff} > 0.4\,\text{MV/cm}$. In the case of gated thermoelectric channels, therefore, SRS is weak. Note that in the calculation of the SRS rates, we have even used relatively large roughness amplitude values of $\Delta_{\text{rms}} = 0.48\,\text{nm}$ and correlation lengths $L_C = 1.3\,\text{nm}$ [54].

The Seebeck coefficient, on the other hand, improves when scattering becomes stronger as shown in Fig. 5b. In general, additional scattering mechanisms improve the Seebeck coefficient since this quantity follows the inverse trend compared to conductivity. Adding SRS to the phonon-limited result of the gated channel improves the Seebeck coefficient at higher carrier concentrations (green-dot lines). Similarly, ionized impurity scattering in the case of the doped channel (solid-black line), largely improves the Seebeck coefficient. That increase, however, is not large enough to compensate for the large degradation of the electrical conductivity caused by ionized impurity scattering.

As a result of the superior conductivity, and only mild reduction in the Seebeck coefficient, the thermoelectric power factor shown in Fig. 5c is much larger in the case of the gated channel compared to the doped channel. The power factor of the gated channel peaks at concentrations around $p \sim 10^{19}/\text{cm}^3$, and it is $\sim 5\times$ higher compared to that of the doped channel. This qualitatively and quantitatively demonstrates the advantage of the gated NW channels for achieving large thermoelectric power factors compared to the traditionally used doped materials. It is again interesting to observe that SRS degrades the power factor of the gated channel only slightly (green-dashed-dot line). On the other hand, IIS is already strong enough at this concentration to cause significant degradation to the power factor of the doped channel (black-solid line).

3 Energy filtering benefits to the power factor of superlattices

The second promising power factor improvement strategy is energy filtering, achieved through introducing energy barriers in the transport direction of electronic charge [37]. Such cross-plane superlattice geometries have indeed demonstrated improvements in the Seebeck coefficient [20,43]. However, no significant improvement in the thermoelectric power factor σS^2 of such structures have been achieved to date. This is because in practice energy barriers also strongly reduce the electrical conductivity, although theoretical studies indicate that this should be possible [23,37,60], and performance improvements to the power factor up to $\sim 40\,\%$ can potentially be achieved. One of the reasons for the inability of experiment to observe power factor improvements is the fact that several design components need to be controlled and optimized in order for the power factor benefits to materialize. Below, we revise these main design features as illustrated in the works of us and others. Using NEGF quantum mechanical transport simulations we demonstrate how power factor improvements can be achieved for 1D and 2D superlattices.

In previous theoretical works [23,24,34,60,61] a series of parameters were identified with regards to the superlattice geometry and the construction of the wells and barriers that provide the highest thermoelectric power factor. These parameters were identified as follows: (i) the carrier energy within the potential wells needs to be semi-relaxed, (ii) the width of the barriers needs to be large enough to prevent tunneling, but small enough to keep the channel resistance low, and (iii) the Fermi level needs to be placed high into the bands for improved conductivity, and $\sim k_B T$ below the maximum of the barriers. With regards to (i), e.g. the size of the well and semi-ballistic transport within them, very large wells will result in diffusive transport, and also reduce the ability of the barriers to produce a high Seebeck coefficient because the barriers will only occupy a small fraction of the total volume of the material. When the wells are too short, on the other hand, although transport within the wells could be ballistic, too many barriers and interfaces are introduced in the geometry, which degrades conductivity substantially. Thus, the optimal case is somewhere in between, which dictates partial energy relaxation of the charge carriers. Note that in general, especially if the structures are highly doped, the carriers' momentum is randomized, and transport is diffusive, but the requirements for large power factors is energy semi-ballisticity, therefore it is acceptable for momentum to be randomized [24,34,60,62]. With regards to (ii), i.e. the role of barrier thickness, Fig. 6 shows the calculated charge current energy flow through a channel with energy barriers. The calculations were performed using Non-Equilibrium-Green's Function (NEGF) simulations, including electron–phonon interactions. The colormap shows the actual current energy

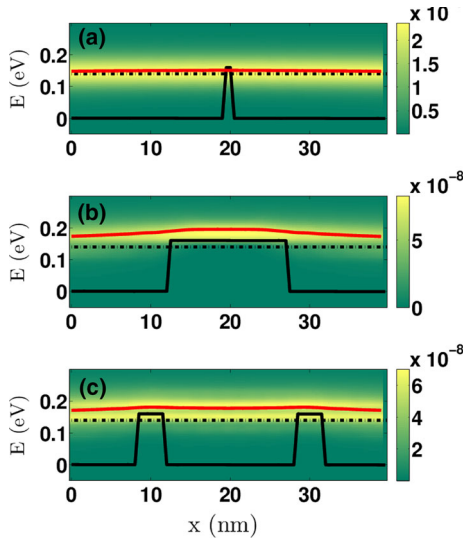

Fig. 6 **a** The band diagram of the superlattice materials under consideration, consisting of a series of potential wells and barriers (*black-solid line*). The Fermi level E_F is indicated by the *black-dashed line*. The *colormap* shows the current energy spectrum through the superlattice material (the average energy of the current is shown by the *red line*). **a** The case of a thin, transparent barrier, in which most current passes through the barrier. **b** The case of a thick barrier, where most of the current passes over the barrier. **c** The case of an optimal superlattice, where most current passed over the barriers, and energy relaxation is observed in the wells (lowering of the *red line* in the well regions). The material is designed to have 50 % ballisticity in electron transport in the wells (Color figure online)

flow with yellow denoting the highest and green the lowest current, while the red line shows the average value of the current energy for the right going carriers. The band profile with the barriers and wells is denoted by the black solid line, and the Fermi level E_F by the black dashed line. Most current flows over the potential barriers as expected, however, carrier energy relaxation due to the emission of optical phonons is observed within the potential wells. Very narrow barriers become transparent to the charge flow and eliminate the Seebeck coefficient (Fig. 6a), and thick barriers cause carriers to relax on the top of that barrier at low energy and velocity states, which hinders the conductivity (Fig. 6b). Thus, barriers as well need to be designed by having this in mind, and for common semiconductor materials such as Si or Ge, this thickness is in the range of a few nanometers (see Fig. 6c).

Following these design guidelines, we perform NEGF quantum transport simulations including the effect of electron scattering with acoustic and optical phonons to illustrate the benefits to the power factor. For simplicity we consider a uniform 1D channel within the effective mass approximation, where the barriers are formed by raising locally the potential. The effect of electron scattering with acoustic and optical phonons in NEGF is modeled by including a self-energy on the diagonal elements of the Hamiltonian. A constant electron–phonon coupling strength D_0 is used for both acoustic and optical phonons as described in detail in

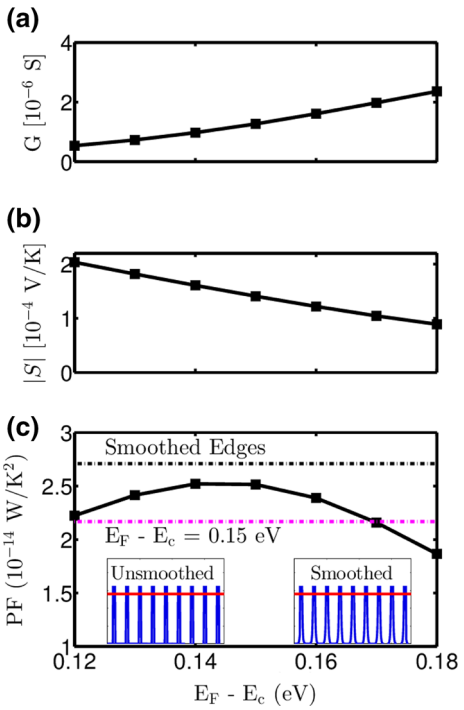

Fig. 7 The thermoelectric coefficients of a 1D superlattice material versus the position of the Fermi level E_F with respect to the conduction band edge. **a** The electrical conductance, **b** the Seebeck coefficient, and **c** the power factor. The barrier height is $V_B = 0.16$ eV. The optimal power factor of the single barrier channel (usual *bulk thermoelectric* operation) is indicated by the *magenta-dashed line*, and the optimal power factor of a superlattice with smoothened barriers by the *black-dashed line* in (**c**). *Insets* of (**c**): The potential profiles in the channel (unsmoothed-sharp barriers and smoothed barriers)

[63,64]. This commonly employed approximation has been shown to capture all essential scattering physics and to be quantitatively valid for many systems [65], such as electrons in silicon [66], transport in carbon nanotubes [64], and many more. We first calibrate the superlattice material under consideration as follows: We set the well widths at $L_W = 20$ nm and find the position of the Fermi level at $E_F = 0.14$ eV above the conduction band edge, which gives the highest ballistic conductance. We then include electron–phonon scattering, and set the value of D_0 such that the conductance of a 20 nm channel is found to be 50 % of the ballistic value. This effectively amounts to fixing a mean free path of 20 nm for the system. The appropriate D_0 was found to be $D_0 = 0.0016$ eV^2 (which, again, for simplicity is taken to be the same for acoustic and optical phonons). Then we introduce the barrier thicknesses of $L_B = 3$ nm using perfect square shaped wells/barriers. We set the barrier height at $V_B = 0.16$ eV ($\sim k_B T$ above E_F).

The power factor, GS^2, was obtained from the current expression:

$$I = G\Delta V + SG\Delta T. \tag{6}$$

For each value of the power factor that was calculated, the simulation was run twice, initially with a small potential difference and no temperature difference ($\Delta T = 0$), which yields the conductance ($G = I_{(\Delta T=0)}/\Delta V$), then again with a small temperature difference and no potential difference ($\Delta V = 0$), which yields the Seebeck coefficient ($S = I_{(\Delta V=0)}/G\Delta T$). This method is validated in Ref. [23]. We used current conservation throughout the system as the convergence criteria to determine self-consistency of the scattering self-energy down to 1 %. The sharp features of the system required an unusually large number (~ 1000 s) of convergence steps that determine the electron–phonon interaction and the Green's function.

By fixing the geometry and the barrier heights V_B as described above, Figure 7 shows the electrical conductance, the Seebeck coefficient, and the power factor of the superlattice structure versus the position of the Fermi level. The magenta line in Fig. 7c shows the maximum power factor that can be achieved using the uniform material without the barriers, in which case the Fermi lever is placed $\sim k_B T$ below the conduction band edge E_C, which operates under the usual bulk thermoelectric principle. Comparison between the two channels (single versus multiple barriers) demonstrates the advantages of the multi-barrier/well geometry to the power factor. The benefit arises because the wells of the channel allow for high energy carriers with increased velocities, compared to low energy carriers in the single barrier geometry [24,34]. The wells locally increase the conductance, but reduce the Seebeck coefficient. The presence of the barriers reduces the electrical conductivity, but increases the Seebeck coefficient. Overall, however, the superlattice geometry provides a power factor advantage by ~ 20 %. It is important to note that the gains are obtained when the Fermi level is positioned at $E_F = 0.14$ eV, which is roughly $\sim k_B T$ below the barrier V_B as also observed in other works [23,24]. This difference between E_F and V_B is the ideal such that the high energetic carriers can still go through the barrier whereas the low energy carriers are blocked, and thus energy filtering is effective, and on the other hand the barriers are not so high as to obscure carrier transport significantly and reduce the conductance. In addition, as explained in Ref. [34,60], the positioning of the Fermi level high into the conduction band allows the use of high velocity carriers, which improve the conductivity of the channel. Another interesting fact, is that perfectly sharp edges are not the ideal barrier features for optimal power factor. The reason is that sharp edges introduce strong quantum reflections, which degrade the electronic conductivity more than they increase the Seebeck coefficient [60]. Figure 7c shows the optimal power factor that can be obtained once the low energy parts of the barriers are smoothened out, which provides an additional improvement (up to ~ 27 %) in total compared to the uniform material. As shown in Ref. [60], it is expected that an additional benefit

even up to $\sim 40\,\%$ could also be obtained when the top edges are smoothened. Thus, when fabricating superlattices, perfect interfaces between the two materials that get connected are not the optimal design, which is good news considering the experimental challenges in achieving perfect interfaces.

After the illustration of power factor gains in a 1D example material, we extend this study in a 2D material, again using the same method, i.e. NEGF simulations for electronic transport including the effect of electron–phonon interactions. In this case we extend the width of the channel in the transverse direction to $W = 30\,\text{nm}$, while the length is kept at $L_{\text{ch}} = 180\,\text{nm}$ as before, with well lengths of $L_{\text{W}} = 20\,\text{nm}$. In this case, several transverse bands appear, but of course extending the width to hundreds of nanometers to reach a realistic 2D material would require an excessively higher computational time. As an indication, the simulation for the NEGF transport in the 1D channel including electron-acoustic and electron-optical phonon interactions requires several hours on a single processor. In the case of the 2D channel, the simulation takes around a day on a 16 core shared memory environment.

For the purposes of this study, we keep the Fermi level constant at $E_{\text{F}} = 0.14\,\text{eV}$, and we examine the influence of the different barrier heights V_{B} and barrier thicknesses L_{B} on the power factor. Figure 8 shows the simulation results for the thermoelectric coefficients. Figure 8a shows the electrical conductance G, Fig. 8b the Seebeck coefficient S, and Fig. 8c the power factor GS^2 versus the thickness of the barrier. Simulation data for three different barrier heights V_{B}, 0.1, 0.12, and 0.14 eV are presented. An important observation, as also mentioned earlier in the case of the 1D case study, is that the power factor peaks at barrier thicknesses of around $L_{\text{B}} = 2\,\text{nm}$. For barrier thicknesses below 2 nm the conductivity increases significantly due to tunneling, but this is detrimental to the Seebeck coefficient. For thicknesses above 2 nm, the low energy/velocity carriers on top of the barriers increase the resistance of the overall material. The power factor peaks somewhere around $L_{\text{B}} = 2\,\text{nm}$. Thus, the optimal barrier needs to be thick enough for tunneling to be prevented, but thin enough for its resistance to remain low [60].

Another important observation is the behavior of the maximum power factor with respect to the barrier height V_{B}. In this case, the highest power factor is observed for barrier heights not $\sim k_{\text{B}}T$ higher compared to the Fermi level as in the 1D channel case, but at $V_{\text{B}} = 0.12$, which is $\sim k_{\text{B}}T$ *below* the Fermi level ($E_{\text{F}} = 0.14\,\text{eV}$). The reason is that the optimal positioning of the barriers compared to the Fermi level is determined by the interplay between the conductance reduction by the barriers and Seebeck increase by energy filtering. This is ultimately controlled by the energy distribution of the carriers and the energy distribution of the different scattering mechanisms that take place. This is different in 1D and 2D cases due to the many more subbands in the 2D case,

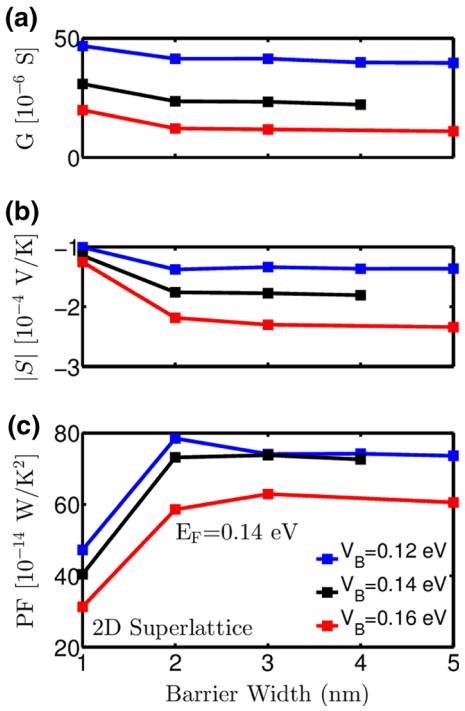

Fig. 8 The thermoelectric coefficients of a 2D superlattice material versus the barrier region thickness (width) L_{B}. **a** The electrical conductance, **b** the Seebeck coefficient, and **c** the power factor. The Fermi level is fixed at $E_{\text{F}} = 0.14\,\text{eV}$, and results for different barrier height situations are shown from $V_{\text{B}} = 0.12\,\text{eV}$ (*blue*) to $V_{\text{B}} = 0.16\,\text{eV}$ (*red*) (Color figure online)

and thus the overall different energy distribution of carriers. (Here we consider that by increasing the width of the channel (in the transverse direction) the electronic structure of the channel deviates from 1D towards 2D). Thus, the various subbands that appear as the transverse direction width of the channel increases provide a different optimized position of the barriers with respect to the Fermi level. In the case of semiclassical transport, all this information is included in the so-called transport distribution (TD) function which appears in the Boltzmann Transport Equation (BTE) as described in [19,58]. For example, a 3D semiclassical study in Ref. [60], which also considered the effect of ionized impurity scattering (which results in very different TD function) showed that the optimal E_{F} is actually $\sim 2k_{\text{B}}T$ below the V_{B}. In that case, the optimal power factor using energy filtering was 40 % higher compared to that of the bulk material. Thus, the message to be conveyed by this finding, is that the design of nanostructured superlattices for enhanced power factors depends on the energetics of the bandstructure and the scattering mechanisms, and can vary by $\pm k_{\text{B}}T$ or even $2k_{\text{B}}T$, which is quite significant, and could mean very different doping conditions needed to place E_{F} precisely achieve the peak of the power factor. Careful considerations of all parameters discussed are needed in order to achieve power factor benefits, which can be extracted through detailed modeling

and simulation works. This, together with the geometrical details of the superlattice construction could explain why to-date experiments were not able to utilize energy filtering and successfully demonstrate power factor improvements in superlattices, despite theoretical predictions.

4 Discussion

The results of Figs. 7 and 8 clearly show that well-designed superlattices could result in ∼20–30% thermoelectric power factor improvements compared to materials with a uniform underlying potential. For this, a series of parameters needs to be carefully calibrated as mentioned earlier (i.e. semi-ballistic wells, proper positioning of the Fermi level with respect to the barriers, proper barrier thickness). Large effort is currently being devoted in achieving high power factors in such geometries, and in this work, we stress the importance in using the proper parameters if these gains are to be achieved, which would come out of advanced simulations. We also need to stress that superlattices and nanocomposites in general, provide high *ZT* figures of merit as a consequence of their extremely low thermal conductivities [37,67–69], as well as the non-uniformity of the spatial thermal conductivity [24,34]. These in and of themselves suggest they are indeed very promising thermoelectric materials. Achieving additional power factor benefits through energy filtering, however, seems to require additional consideration of several other design parameters [70,71].

It is interesting to consider topologies and material designs which *combine* the two promising directions described in this paper, modulation doping and energy filtering. In this way, very large power factors can be achieved. One demonstration is our recent work in nanocrystalline materials presented in Ref. [34,72,73]. In that case, two-phase material geometries consisting of grains of diameter ∼ 30 nm, separated by grain boundaries of thickness ∼ 2 nm, which form barriers [74,75] and provide energy filtering were demonstrated. Significant power factor improvements can be achieved once the underlying nanostructure is properly designed to incorporate three important effects: (*i*) Degenerate doped grain regions (potential wells) at concentrations up to the $p = 1.2 \times 10^{20}/\mathrm{cm}^3$ to achieve overall high conductivity, i.e. the Fermi level is raised significantly into the bands; (*ii*) Highly non-uniform placement of the dopants, preferentially in the middle of the grains (introducing partially modulation doping); and (*iii*) Potential barriers around the grain boundary regions to achieve carrier filtering and to improve the Seebeck coefficient. The result is that the power factor in this material largely overpasses the power factor of bulk crystalline Si by at least ∼ 5× reaching values of ∼ 15 mW/mK (compared to the bulk Si value ∼ 2 mW/mK), demonstrating one of the highest power factors reported at room temperature.

5 Conclusions

In conclusion, despite the large improvement in thermoelectric performance over the last 20 years due to the realization of materials with extremely low thermal conductivities, it is now recognized that any further improvements will come from the power factor. Out of several strategies to achieve high power factors, in this paper we discuss two of the most promising ones, namely modulation doping and energy filtering. Modulation doping, in terms of remote doping, or electrostatic gating, allows for high carrier mobilities and conductivities at the high carrier densities required to maximize the power factor, because they free the channel of the degrading effect of ionized impurity scattering. We show that power factors up to 5× compared to those of doped channels can be achieved. The limitation of this techniques, however, is that improvements can only be realized in the material regions in which the electric field from the remote dopants, or the gate, can extend, which might limit its expansion to large volumes. Energy filtering allows improvement of the Seebeck coefficient and the power factor in structures with embedded potential barriers, such as the case of superlattices studied in this review. A series of barriers and wells can be carefully designed such that up to ∼ 27 % benefits to the power factor can be realized. Indeed, a material that combine these two strategies has been shown to provide one of the highest power factor reported (∼ 15 mW/mK) [34]. In general, however, increasing the thermoelectric power factor, also for materials with ultra-low thermal conductivities, remains to be a major challenge for the thermoelectric community. Success in surpassing the adverse interdependence of the electrical conductivity and the Seebeck coefficient and achieve high power factors, however, will possibly allow for materials with *ZT*s beyond the value of 3, and enlarge the range of applications and use for thermoelectricity.

Acknowledgments Mischa Thesberg was supported by the Austrian Science Fund (FWF) contract P25368-N30. Some of the computational results presented have been achieved in part using the Vienna Scientific Cluster (VSC).

References

1. Vining, C.B.: An inconvenient truth about thermoelectrics. Nat. Mater. **8**, 83–85 (2009)
2. Poudel, B., Hao, Q., Ma, Y., Lan, Y., Minnich, A., Yu, B., Yan, X., Wang, D., Muto, A., Vashaee, D., Chen, X., Liu, J., Dresselhaus, M.S., Chen, G., Ren, Z.: Science **320**, 634 (2008)
3. Wu, H.J., Zhao, L.-D., Zheng, F.S., Wu, D., Pei, Y.L., Tong, X., Kanatzidis, M.G., He, J.Q.: Broad temperature plateau for thermoelectric figure of merit ZT > 2 in phase-separated $PbTe_{0.7}S_{0.3}$. Nat. Commun **5**, 5515 (2014)
4. Biswas, K., He, J., Zhang, Q., Wang, G., Uher, C., Dravid, V.P., Kanatzidis, M.G.: Strained endotaxial nanostructures with high thermoelectric figure of merit. Nat. Chem. **3**, 160–166 (2011)

5. Pei, Y., Shi, X., LaLonde, A., Wang, H., Chen, L., Snyder, G.J.: Convergence of electronic bands for high performance bulk thermoelectrics. Nature **473**, 66–69 (2011)
6. Zhao, L.-D., Lo, S.-H., Zhang, Y., Sun, H., Tan, G., Uher, C., Wolverton, C., Dravid, V.P., Kanatzidis, M.G.: Ultralow thermal conductivity and high thermoelectric figure of merit in SnSe crystals. Nature **508**, 373–377 (2014)
7. Hochbaum, A.I., Chen, R., Delgado, R.D., Liang, W., Garnett, E.C., Najarian, M., Majumdar, A., Yang, P.: Enhanced thermoelectric performance of rough silicon nanowires. Nature **451**, 163–167 (2008)
8. Boukai, A.I., Bunimovich, Y., Kheli, T., Yu, J.-K., Goddard III, W.A., Heath, J.R.: Silicon nanowires as efficient thermoelectric materials. Nature **451**, 168–171 (2008)
9. Li, D., Wu, Y., Fang, R., Yang, P., Majumdar, A.: Thermal conductivity of Si/SiGe superlattice nanowires. Appl. Phys. Lett. **83**, 3186 (2003)
10. Chen, G.: Phonon transport in low-dimensional structures. Semicond. Semimet. **71**, 203–259 (2001)
11. Chen, R., Hochbaum, A.I., Murphy, P., Moore, J., Yang, P., Majumdar, A.: Thermal conductance of thin silicon nanowires. Phys. Rev. Lett. **101**, 105501 (2008)
12. Li, D., Huxtable, S.T., Abramsin, A.R., Majumdar, A.: Thermal transport in nanostructured solid-state cooling devices. Trans. ASME **127**, 108–114 (2005)
13. Martin, P., Aksamija, Z., Pop, E., Ravaioli, U.: Impact of phonon-surface roughness scattering on thermal conductivity of thin Si nanowires. Phys. Rev. Lett. **102**, 125503 (2009)
14. Biswas, K., He, J., Blum, I.D., Wu, C.-I., Hogan, T.P., Seidman, D.N., Dravid, V.P., Kanatzidis, M.G.: High-performance bulk thermoelectrics with all-scale hierarchical architectures. Nature **489**, 414–418 (2012)
15. Garg, J., Chen, G.: Minimum thermal conductivity in superlattices: a first-principles formalism. Phys. Rev. B **87**, 140302 (2013)
16. Nielsch, K., Bachmann, J., Kimling, J., Böttner, H.: Thermoelectric nanostructures: from physical model systems towards nanograined composites. Adv. Energy Mater. **1**, 713–731 (2011)
17. Vineis, C.J., Shakouri, A., Majumdar, A., Kanatzidis, M.C.: Nanostructured thermoelectrics: big efficiency gains from small features. Adv. Mater. **22**, 3970–3980 (2010)
18. Hicks, L.D., Dresselhaus, M.S.: Thermoelectric figure of merit of a one-dimensional conductor. Phys. Rev. B **47**, 16631 (1993)
19. Mahan, G.D., Sofo, J.O.: The best thermoelectric. Proc. Natl. Acad. Sci. USA **93**, 7436–7439 (1996)
20. Zeng, G., Bowers, J.E., Zide, J.M.O., Gossard, A.C., Kim, W., Singer, S., Majumdar, A., Singh, R., Bian, Z., Zhang, Y., Shakouri, A.: ErAs:InGaAs/InGaAlAsErAs:InGaAs/InGaAlAs superlattice thin-film power generator array. Appl. Phys. Lett. **88**, 113502 (2006)
21. Neophytou, N., Kosina, H.: Effects of confinement and orientation on the thermoelectric power factor of silicon nanowires. Phys. Rev. B **83**, 245305 (2011)
22. Neophytou, N., Kosina, H.: On the interplay between electrical conductivity and seebeck coefficient in ultra-narrow silicon nanowires. J. Electron. Mater. **41**(6), 1305–1311 (2012)
23. Kim, R., Lundstrom, M.: Computational study of the Seebeck coefficient of one-dimensional composite nano-structures. J. Appl. Phys. **110**, 034511 (2011)
24. Kim, R., Lundstrom, M.S.: Computational study of energy filtering effects in one-dimensional composite nano-structures. J. Appl. Phys. **111**, 024508 (2012)
25. Zebarjadi, M., Joshi, G., Zhu, G., Yu, B., Minnich, A., Lan, Y., Wang, X., Dresselhaus, M., Ren, Z., Chen, G.: Enhancement of thermoelectric properties by modulation-doping in silicon germanium alloy nanocomposites. Nano Lett. **11**, 2225–2230 (2011)
26. Yu, B., Zebarjadi, M., Wang, H., Lukas, K., Wang, H., Wang, D., Opeil, C., Dresselhaus, M., Chen, G., Ren, Z.: Nano Lett. **12**(4), 2077–2082 (2012)
27. Curtin, B.M., Codecido, E.A., Krämer, S., Bowers, J.E.: Field-effect modulation of thermoelectric properties in multigated silicon nanowires. Nano Lett. **13**, 5503–5508 (2013)
28. Neophytou, N., Kosina, H.: Gated Si nanowires for large thermoelectric power factors. Appl. Phys. Lett. **105**, 073119 (2014)
29. Samarelli, A., Llin, FerreL, Cecchi, S., Frigerio, J., Etzelstorfer, T., Müller, E., Zhang, Y., Watling, J.R., Chrastina, D., Isella, G., Stangl, J., Hague, J.P., Weaver, J.M.R., Dobson, P., Paul, D.J.: The thermoelectric properties of Ge/SiGe modulation doped superlattices. J. Appl. Phys. **113**, 233704 (2013)
30. Hou, Q.R., Gu, B.F., Chen, Y.B., He, Y.J., Sun, J.L.: Enhancement of the thermoelectric power factor of $MnSi_{1.7}$ film by modulation doping of Al and Cu. Appl. Phys. A **114**, 943–949 (2014)
31. Pei, Y.-L., Wu, H., Wu, D., Zheng, F., He, J.: High thermoelectric performance realized in a BiCuSeO system by improving carrier mobility through 3D modulation doping. J. Am. Chem. Soc. **136**, 13902 (2014)
32. Jaworski, C.M., Kulbachinskii, V., Heremans, J.P.: Antimony as an amphoteric dopant in lead telluride. Phys. Rev. B **80**, 125208 (2009)
33. Popescu, A., Woods, L.M., Martin, J., Nolas, G.S.: Model of transport properties of thermoelectric nanocomposite materials. Phys. Rev. B **79**, 205302 (2009)
34. Neophytou, N., Zianni, X., Kosina, H., Frabboni, S., Lorenzi, B., Narducci, D.: Simultaneous increase in electrical conductivity and Seebeck coefficient in highly boron-doped nanocrystalline Si. Nanotechnology **24**, 205402 (2013)
35. Thesberg, M., Pourfath, M., Kosina, H., Neophytou, N.: The influence of non-idealities on the thermoelectric power factor of nanostructured superlattices. J. Appl. Phys **118**, 224301 (2015)
36. Thesberg, M., Pourfath, M., Neophytou, N., Kosina, H.: The fragility of thermoelectric power factor in cross-plane superlattices in the presence of nonidealities: a quantum transport simulation approach. J. Electron. Mater., online (2015)
37. Vashaee, D., Shakouri, A.: Improved thermoelectric power factor in metal-based superlattices. Phys. Rev. Lett. **92**, 106103 (2004)
38. Zhao, L.D., Lo, S.H., He, J.Q., Hao, L., Biswas, K., Androulakis, J., Wu, C.I., Hogan, T.P., Chung, D.Y., Dravid, V.P., Kanatzidis, M.G.: High performance thermoelectrics from earth-abundant materials: enhanced figure of merit in PbS by second phase nanostructures. J. Am. Chem. Soc. **133**, 20476–20487 (2011)
39. Bahk, J.-H., Bian, Z., Shakouri, A.: Electron transport modeling and energy filtering for efficient thermoelectric $Mg_2Si_{1-x}Sn_x$ solid solutions. Phys. Rev. B **89**, 075204 (2014)
40. Bahk, J.-H., Shakouri, A.: Enhancing the thermoelectric figure of merit through the reduction of bipolar thermal conductivity with heterostructure barriers. Appl. Phys. Lett. **105**, 052106 (2014)
41. Narducci, D., Selezneva, E., Cerofolini, G., Frabboni, S., Ottaviani, G.: Impact of energy filtering and carrier localization on the thermoelectric properties of granular semiconductors. J. Solid State Chem. **193**, 19–25 (2012)
42. Liu, W., Yan, X., Chen, G., Ren, Z.: Recent advances in thermoelectric nanocomposites. Nano Energy **1**, 42–56 (2012)
43. Zide, J.M.O., Vashaee, D., Bian, Z.X., Zeng, G., Bowers, J.E., Shakouri, A., Gossard, A.C.: Demonstration of electron filtering to increase the Seebeck coefficient in $In_{0.53}Ga_{0.47}As/In_{0.53}Ga_{0.28}Al_{0.19}$ as superlattices. Phys. Rev. B **74**, 205335 (2006)
44. Shakouri, A.: Recent developments in semiconductor thermoelectric physics and materials. Annu. Rev. Mater. Res. **41**, 399–431 (2011)

45. Alam, H., Ramakrishna, S.: Nonequilibrium green's function treatment of phonon scattering in carbon-nanotube transistors. Nano Energy **2**, 190–212 (2013)
46. Tian, Y., Sakr, M.R., Kinder, J.M., Liang, D., MacDonald, M.J., Qiu, R.L.J., Gao, H.-J., Gao, X.P.A.: One-dimensional quantum confinement effect modulated thermoelectric properties in inas nanowires. Nano Lett. **12**, 6492–6497 (2012)
47. Moon, J., Kim, J.-H., Chen, Z.C.Y., Xiang, J., Chen, R.: Gate-modulated thermoelectric power factor of hole gas in Ge–Si core-shell nanowires. Nano Lett. **13**, 1196–1202 (2013)
48. Liang, W., Hochbaum, A.I., Fardy, M., Rabin, O., Zhang, M., Yang, P.: Field-effect modulation of Seebeck coefficient in single PbSe nanowires. Nano Lett. **9**, 1689–1693 (2009)
49. Neophytou, N., Baumgartner, O., Stanojevic, Z., Kosina, H.: Non-equilibrium green's function treatment of phonon scattering in carbon-nanotube transistors. Solid State Electron. **90**, 44–50 (2013)
50. Boykin, T.B., Klimeck, G., Oyafuso, F.: Valence band effective-mass expressions in the sp3d5s* empirical tight-binding model applied to a Si and Ge parametrization. Phys. Rev. B **69**, 115201 (2004)
51. Neophytou, N., Paul, A., Lundstrom, M., Klimeck, G.: Bandstructure effects in silicon nanowire electron transport. IEEE Trans. Electron. Dev. **55**, 1286–1297 (2008)
52. Lee, S., Oyafuso, F., Von Allmen, P., Klimeck, G.: Boundary conditions for the electronic structure of finite-extent embedded semiconductor nanostructures. Phys. Rev. B **69**, 045316 (2004)
53. Neophytou, N., Kosina, H.: Large enhancement in hole velocity and mobility in p-type [110] and [111] silicon nanowires by cross section scaling: an atomistic analysis. Nano Lett. **10**, 4913–4919 (2010)
54. Jin, S., Fischetti, M.V., Tang, T.: Modeling of electron mobility in gated silicon nanowires at room temperature: surface roughness scattering, dielectric screening, and band nonparabolicity. J. Appl. Phys. **102**, 083715 (2007)
55. Sakaki, H., Noda, T., Hirakawa, K., Tanaka, M., Matsusue, T.: Interface roughness scattering in GaAs/AlAs quantum wells. Appl. Phys. Lett. **51**, 1934 (1987)
56. Uchida, K., Takagi, S.: Carrier scattering induced by thickness fluctuation of silicon-on-insulator film in ultrathin-body metal-oxide-semiconductor field-effect transistors. Appl. Phys. Lett. **82**, 2916 (2003)
57. Ramayya, E.B., Vasileska, D., Goodnick, S.M., Knezevic, I.: Electron transport in silicon nanowires: the role of acoustic phonon confinement and surface roughness scattering. J. Appl. Phys. **104**, 063711 (2008)
58. Neophytou, N., Kosina, H.: Atomistic simulations of low-field mobility in Si nanowires: influence of confinement and orientation. Phys. Rev. B **84**, 085313 (2011)
59. Rameshan, K., Wong, N.A., Chan, K., Sim, S.P., Yang, C.Y.: Modeling inversion-layer carrier mobilities in all regions of MOSFET operation. Solid-State Electron. **46**, 153–156 (2002)
60. Neophytou, N., Kosina, H.: Optimizing thermoelectric power factor by means of a potential barrier. J. Appl. Phys. **114**, 044315 (2013)
61. Nishio, Y., Hirano, T.: Improvement of the efficiency of thermoelectric energy conversion by utilizing potential barriers. Jpn. J. Appl. Phys. **36**, 170–174 (1997)
62. Kim, R., Jeong, C., Lundstrom, M.S.: On momentum conservation and thermionic emission cooling. J. Appl. Phys. **107**, 054502 (2010)
63. Datta, S.: Electronic Transport in Mesoscopic Systems. Cambridge University Press, Cambridge (1997)
64. Koswatta, S.O., Hasan, S., Lundstrom, M.S., Anantram, M.P., Nikonov, D.E.: Nonequilibrium green's function treatment of phonon scattering in carbon-nanotube transistors. IEEE Trans. Electron. Dev. **54**, 2339–2351 (2007)
65. Price, A., Martinez, A., Valin, R., Barker, J.R.: Impact of different electron-phonon scattering models on the electron transport in a quantum wire. J. Phys.: Conf. Ser. **526**, 012007 (2014)
66. Rhyner, R., Luisier, M.: Phonon-limited low-field mobility in silicon: quantum transport vs. linearized Boltzmann transport equation. J. Appl. Phys. **114**, 223708 (2013)
67. Venkatasubramanian, R., Siivola, E., Colpitts, T., O' Quinn, B.: Thin-film thermoelectric devices with high room-temperature figures of merit. Nature **413**, 597–602 (2001)
68. Shi, L., Jiang, J., Zhang, G., Li, B.: High thermoelectric figure of merit in silicon–germanium superlattice structured nanowires. Appl. Phys. Lett. **101**, 233114 (2012)
69. Hu, M., Poulikakos, D.: Si/Ge superlattice nanowires with ultralow thermal conductivity. Nano Lett. **12**, 5487–5494 (2012)
70. Saleemi, M., Famengo, A., Fiameni, S., Boldrini, S., Battiston, S., Johnsson, M., Muhammed, M., Toprak, M.S.: Modeling inversion-layer carrier mobilities in all regions of MOSFET operation. J. Alloys Compd. **619**, 31–37 (2015)
71. Perumal, S., Gorsse, S., Ail, U., Prakasam, M., Vivès, S., Decourt, R., Umarji, A.M.: Modeling inversion-layer carrier mobilities in all regions of MOSFET operation. Mater. Lett. **155**, 41–43 (2015)
72. Neophytou, N., Zianni, X., Kosina, H., Frabboni, S., Lorenzi, B., Narducci, D.: J. Electron. Mater. **43**(6), 1896–1904 (2014)
73. Narducci, D., Lorenzi, B., Zianni, X., Neophytou, N., Frabboni, S., Gazzadi, G.C., Roncaglia, A., Suriano, F.: Enhancement of the power factor in two-phase silicon-boron nanocrystalline alloys. Phys. Status Solidi a **211**(6), 1255–1258 (2014)
74. Seto, J.Y.W.: The electrical properties of polycrystalline silicon films. J. Appl. Phys. **46**, 5247 (1975)
75. Orton, J.W., Powell, M.J.: The Hall effect in polycrystalline and powdered semiconductors. Rep. Prog. Phys. **43**, 1263 (1980)